WANG, H., MURZYN, F., and CHANSON, H. (2015). "Interaction between Free-Surface, Two-Phase Flow and Total Pressure in Hydraulic Jump." *Experimental Thermal and Fluid Science*, Vol. 64, pp. 30-41 (DOI: 10.1016/j.expthermflusci.2015.02.003) (ISSN 0894-1777).

Interaction between free-surface, two-phase flow and total pressure in hydraulic jump

Hang Wang ([1]) (*), Frédéric Murzyn ([2]) and Hubert Chanson ([1])
([1]) The University of Queensland, School of Civil Engineering, Brisbane QLD 4072, Australia
([2]) ESTACA Campus Ouest, Parc Universitaire de Laval Changé, BP 53061 Laval Cedex 9, France
(*) Corresponding author: hang.wang@uqconnect.edu.au; +61 4309 49204

Abstract
A hydraulic jump is characterised by intense turbulent flow patterns and substantial flow aeration. The flow turbulence, at both macroscopic and microscopic scales, interacts with the air entrainment process and the free-surface. A series of simultaneous measurements of the free-surface fluctuations, jump toe oscillations, void fraction and total pressure variations allowed for an investigation of the interactions between these characteristics. Experiments were conducted for a range of Froude numbers from 3.8 to 8.5. The total pressure measurements were justified for the air-water flow characterisation of the flow region with a positive time-averaged velocity. The interactions between roller surface deformation, air entrainment and diffusion, velocity variation, flow bulking, and the associated total pressure field modulation highlighted different flow regions, hence flow patterns, in the roller. The jump toe oscillation was found closely linked to the air entrapment at the toe and velocity variation in the shear flow. The instable total pressure distribution was primarily associated with the free-surface fluctuation for the bubbly roller region and with the velocity re-distribution for the lower shear region underneath. The present work provides new information on the physical characteristics of hydraulic jumps and a comprehensive insight into the nature of such complex turbulent two-phase flow.

Keywords
Air-water flow; Total pressure fluctuation; Cross-correlation; Jump roller region; Free-surface fluctuation; Jump toe oscillation

Abbreviations
ADM: acoustic displacement meter; PDP: phase-detection probe; TPP: total pressure probe

1 Introduction
A hydraulic jump is commonly encountered in natural streams and hydraulic structures if a supercritical flow transits to a subcritical regime (Lighthill 1978, Montes 1998). The jump roller is a turbulent two-phase flow region of a hydraulic jump with a recirculating pattern and where large-scale turbulence develops and interacts with free-surface and air entrainment. With a large inflow Froude number, a hydraulic jump is characterised by significant free-surface fluctuations and deformations, substantial singular air entrapment at the jump toe and uncontrolled interfacial aeration at the free-surface, and production of large vortices in which large amount of air is advected downstream. Both flow turbulence and air-water mixing contribute to efficient energy dissipation. Thus hydraulic jumps are broadly used as energy dissipators, fluid mixers and flow re-aerators (e.g. Fig 1) (Hager 1992). Despite the wide application, the detailed flow mechanics in hydraulic jumps remain unclear, even considered in laboratory scales. The complexity of the flow is largely associated with the coexistence of and interaction between turbulence and air entrainment in a wide range of length and time scales. Figure 2a illustrates the main fluctuating nature of hydraulic jump, including the formation of vortical structures and the oscillations of jump toe position and water elevation (Wang & Chanson 2014). Such macro-scale motions are combined with the microscopic

turbulence, leading to temporal variations in the velocity and pressure field. Figure 2b sketches the flow aeration processes. The entrapment of air at the jump toe is observed to be linked to the jump toe oscillation and vortex formation (Long et al. 1991). The convective and diffusive transport of air bubbles, as well as the bubble breakage, grouping and coalescence, is affected by the development of turbulence and buoyancy effects (Chanson 2007). In addition, the strong turbulence and flow aeration hinder the application of many traditional flow measurement techniques such as PIV and LDV.

Figure 1. Hydraulic jump in stilling basin of Paradise dam in Burnett River, Bundaberg QLD, Australia, with rough surface and white water indicating violent flow motions and air-water exchange; Discharge estimated to be in excess of 6300 m^3/s with Reynolds number of 1.9×10^7

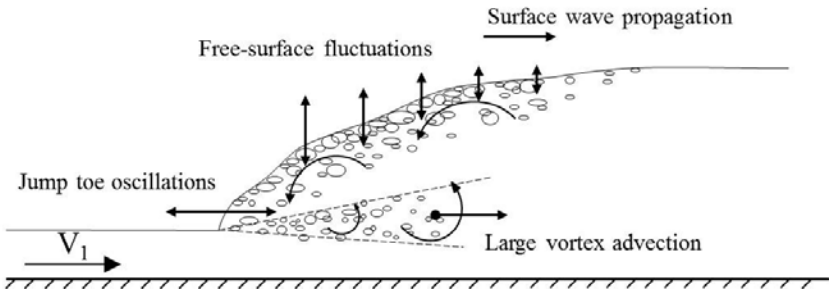

(a)

Figure 2. Large-scale fluctuating motions (a, top) and flow aeration (b, bottom) in hydraulic jump

NB: Figure 2(a) was incorrectly printed in the published manuscript - The above sketch is the correct one.

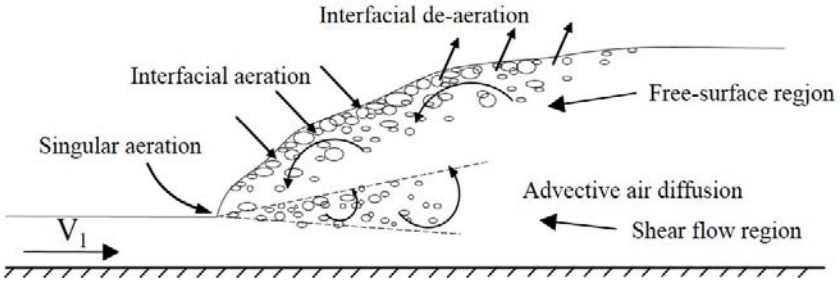

(b)

Figure 2. Large-scale fluctuating motions (a, top) and flow aeration (b, bottom) in hydraulic jump

The study of hydraulic jump dates back to Bidone (1819) and Bélanger (1841). Basic flow characteristics such as the upstream and downstream depths and the length of the jump were the primary focus of early studies before the introduction of hot-film anemometer and conductivity phase-detection probe by Rouse et al. (1959) and Rajaratnam (1962). Such intrusive flow measurement techniques brought insight into the air-water flow and velocity properties. Other early contributions to the two-phase flow investigation included Resch & Leutheusser (1972), Thandaveswara (1974) and Babb & Aus (1981). The description of time-averaged two-phase flow properties were improved in the past two decades with the development of data processing techniques. Chanson (1995) and Chanson & Brattberg (2000) presented typical distributions of void fraction, bubble count rate and interfacial velocity in the jump roller, followed by a series of studies up to date (Murzyn et al. 2005, Chanson 2007,2010, Chachereau & Chanson 2011a, etc.). The free-surface dynamics were measured either intrusively or non-intrusively, showing agreeable results in terms of the free-surface fluctuation amplitude and characteristic frequencies (Mouaze et al. 2005, Murzyn & Chanson 2009, Chachereau & Chanson 2011b). Further observations on the jump toe oscillations were documented by Zhang et al. (2013). Theoretical modelling of the free-surface profile and fluctuating motions were presented by Valiani (1997) and Richard & Gavrilyuk (2013). The interactions between turbulent and air-water flow properties were discussed for some limited flow conditions by means of simultaneous free-surface, bubbly flow and/or turbulence measurements (Cox & Shin 2003, Longo 2010, Wang & Chanson 2014) and bubble clustering behaviours (Chanson 2007). The flow instabilities were also linked to the pressure fluctuations inside and beneath the jump. The pressure measurements first received attention because of its significance in damage prevention of hydraulic structures (Abdul Khader & Elango 1974, Bowers & Toso 1988). While most published works were focused on the pressure quantification on the bottom and sidewalls of hydraulic jump (Vasiliev & Bukreyev 1967, Schiebe 1971, Lopardo & Henning 1985, Toso & Bowers 1988, Farhoud & Narayanan 1991, Fiorotto & Rinaldo 1992), direct measurement of internal pressure field in the roller was almost absent. A recent achievement was brought by Lopardo (2013) proposing a correlation between the turbulence intensity and a pressure fluctuation coefficient, albeit based upon different sets of experiments not undertaken at the same time.

This paper presents new experimental study of the free-surface, air-water flow and total pressure characteristics and interactions in classical hydraulic jumps. Simultaneous measurements of longitudinal jump toe oscillation, vertical free-surface fluctuation, instantaneous void fraction and total pressure were performed. The total pressure fluctuation was related to the instable water level and velocity distribution, and their relationships reflected the different flow patterns in the bottom shear flow and upper free-surface regions of the jump roller.

2 Instrumentation and data processing

2.1 Instrumentation

The main experimental instruments used in the present study included a total pressure probe (TPP), a dual-tip phase-detection probe (PDP) and five acoustic displacement meters (ADMs).

TPP: The total pressure probe measures the stagnation pressure at the probe tip. The miniature pressure transducer (Model MRV21, manufactured by MeasureX, Australia) on the probe tip is a MEMS (Micro-Electro-Mechanical Systems) technology based sensor with a 4-mm-diameter silicon diaphragm. Mechanical signals induced by the pressure on the diaphragm are transduced to electronic signals, with a response frequency up to 100 kHz. The measurement range is from vacuum to 50 kPa above atmospheric pressure. An amplification unit was connected to the total pressure probe to output voltage signals up to 1 V and filter the electronic noise above 2 kHz. A daily static and dynamic calibration of the total pressure probe was recommended because the output voltage appeared to be temperature or ambient-pressure sensitive.

PDP: The dual-tip phase-detection probe detects the air-water interfaces with its needle sensors based upon the different electrical conductivities of air and water. The phase-detection probe is equipped with two parallel needle sensors (inner diameter: 0.25 mm, outer diameter: 0.8 mm) with a transverse separation distance of 2.2 mm. The leading sensor is 7.25 mm longer than the trailing sensor, and the two sensors are designed to pierce bubbles or droplets one after the other. The probe was excited with a response time less than 10 μs. A high-voltage output was recorded when the sensor tip is in water, while a low-voltage output was given in air. The voltage signal was converted to instantaneous void fraction data based upon a single threshold selected at 50% between the upper and lower maximum voltage probabilities (thus corresponding to water and air phases respectively).

ADM: The acoustic displacement meter measures the distance between the sensor and the detected water surface by emitting acoustic beams and receiving the reflected ones. Two models of sensors were used, i.e. Microsonic^{TM} Mic+35/IU/TC and Mic+25/IU/TC. The former provided a measurement range between 60 and 350 mm and a response time less than 70 ms, used herein for the measurement of longitudinal jump front position. The latter gave a measurement range from 30 to 250 mm and a response time less than 50 ms, and was used to record the vertical water elevation. The severe water surface deformation and splashing resulted in some erroneous samples in the voltage signal, which were removed manually in pre-processing.

2.2 Facility and experimental setup

Hydraulic jumps were generated in a 3.2 m long, 0.5 m wide horizontal channel with a smooth HDPE bed and 0.4 m high glass sidewalls. Water was supplied from a constant head reservoir into the upstream head tank of the channel, the flow rate being measured with a Venturi meter with accuracy of 2%. Horizontal impinging flow was discharged into the flume through a rounded undershoot gate of the tank. The downstream flow conditions were controlled with an overshoot sluice gate at the end of the channel. The inflow depth was measured using a point gauge. The accuracy of inflow depth reading depended upon the maximum between free-surface roughness and precision of the gauge (0.2 mm) for different flow conditions.

All measurements were performed on the channel centreline. The instrumental setup is shown in Figure 3. Four acoustic displacement meters measured the water elevations of the free-surface, and one displacement meter was placed horizontally over the inflow water surface, with the sensor head facing the oscillating jump front. The distance between the roller surface and each displacement meter was adjusted within 0.15 – 0.25 m to fit the sensor measurement range, and any two sensors

were separated by over 0.12 m to avoid cross-talking between the sensors. The total pressure probe and phase-detection probe were mounted side by side with a 9-mm transverse distance between the tips. They were sampled at the same longitudinal and vertical positions right below one of the acoustic displacement meters above. While a trolley spanning over the channel provided support to the probes and facilitated data collection at different vertical positions, the positions of the displacement meters were fixed for each series of measurements in a vertical cross-section. All instruments were sampled simultaneously at 5 kHz for 180 s at each measurement point. Further details were provided in Wang et al. (2014b).

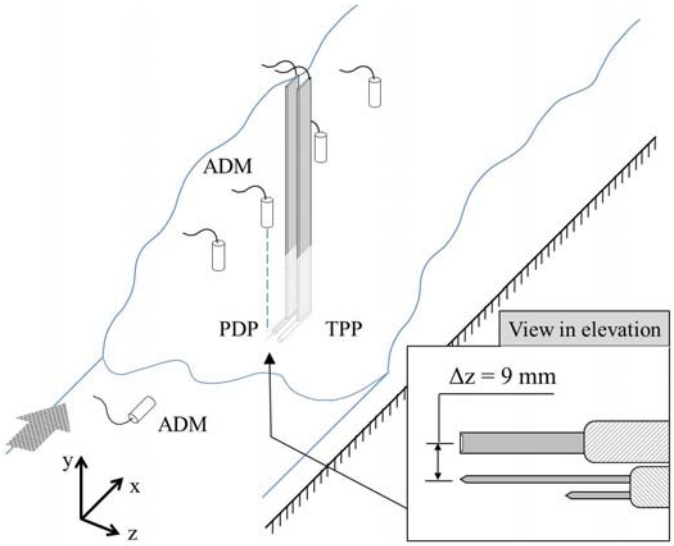

(a)

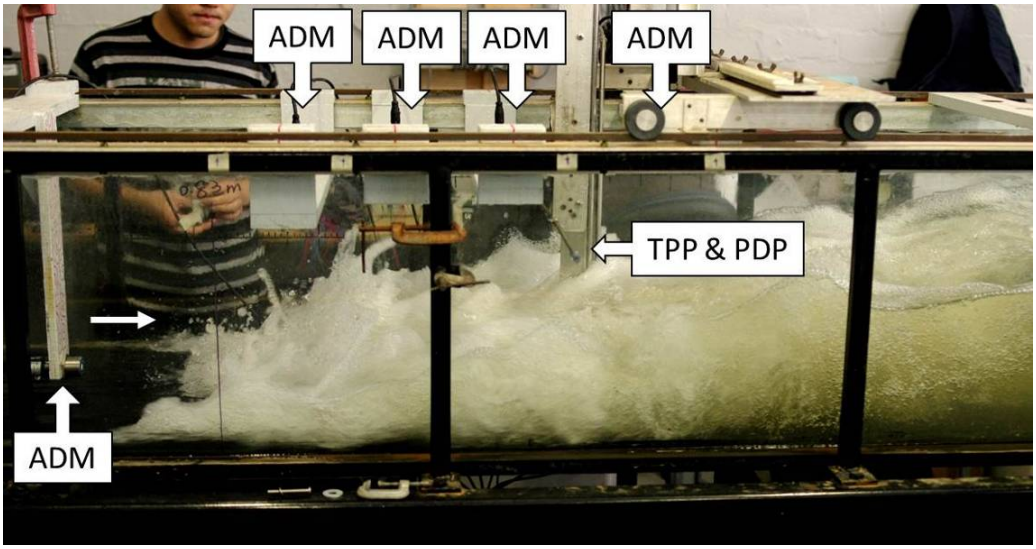

(b)

Figure 3. Setup of instruments: (a, top) sketch and (b, bottom) photograph for flow rate Q = 0.0397 m^3/s, inflow depth d_1 = 0.0208 m, longitudinal jump toe position x_1 = 0.83 m, inflow Froude number Fr_1 = 8.5 and Reynolds number Re = 8.0×10^4

2.3 Processing of simultaneous measurement signals

A correlation analysis of the simultaneously sampled signals provided some information of the coupling between the corresponding flow properties. Murzyn & Chanson (2009), Chachereau &

Chanson (2011b) and Wang & Chanson (2014) performed earlier investigations in terms of the correlation between instantaneous void fraction and local water elevations. Herein the investigations were broadened to cover the longitudinal jump toe oscillation, vertical free-surface fluctuation, instantaneous void fraction c and total pressure p. Denoting x and y as the longitudinal and vertical water surface position signals respectively, a series of correlation functions $R_{ij}(\tau)$ ($i,j = x,y,c,p$) were obtained, where the subscripts refer to the correlated signals in order and τ is the time lag. Table 1 lists the relevant flow properties corresponding to each correlation function. Note that $R_{xy}(\tau)$ between the horizontal and vertical free-surface motions was independent of the vertical positions of total pressure and phase-detection probes, while the rest correlations were functions of the elevation in jump roller.

Table 1. Summary of correlated simultaneous signals and corresponding filtering cut-off frequencies

Symbol	Correlated signals	Instruments	Signal filtering cut-off frequency
R_{xy}	1. instantaneous jump toe position 2. instantaneous water surface depth	Acoustic displacement meter Acoustic displacement meter	0 – 50 Hz
R_{xc}	1. instantaneous jump toe position 2. instantaneous void fraction	Acoustic displacement meter Phase-detection probe	0 – 50 Hz
R_{yc}	1. instantaneous water surface depth 2. instantaneous void fraction	Acoustic displacement meter Phase-detection probe	0 – 50 Hz
R_{xp}	1. instantaneous jump toe position 2. instantaneous total pressure	Acoustic displacement meter Total pressure probe	0 – 50 Hz
R_{yp}	1. instantaneous water surface depth 2. instantaneous total pressure	Acoustic displacement meter Total pressure probe	0 – 50 Hz
R_{pc}	1. instantaneous total pressure 2. instantaneous void fraction	Total pressure probe Phase-detection probe	0 – 2000 Hz

The signals of the acoustic displacement meters, phase-detection probe and total pressure probe were pre-processed prior to the correlation. Figure 4 demonstrates different stages of the data processing using a pair of 5-s ADM and PDP signal segments. Figure 4a shows the raw signals. Erroneous samples caused by large free-surface deformation and splashing were removed from the ADM signal. The number of erroneous points increased with increasing Froude number and reached up to 3% of total samples for the largest Froude number. All voltage signals were converted, respectively, into water depth data, binary instantaneous void fraction data ($c = 0$ for water and $c = 1$ for air) and total pressure data (Fig 4b). When the ADM signal was involved, the correlated signals were filtered down to 50 Hz to match the relatively slow response of the displacement meters. Otherwise, for the correlation between instantaneous void fraction and total pressure, the signals were filtered to 2 kHz because any high-frequency component above 2 kHz in the pressure signal was eliminated by the amplification system (Table 1). The filtered data were smoothed over every 100 points for the 50 Hz signals and over every 2.5 points for the 2 kHz signals (Fig 4c). Lastly, they were linearly interpolated with constant intervals to enable the cross-correlation calculation. Each 180-s pre-processed signal was evenly divided into six non-overlapping segments. The cross-correlation functions were calculated for all segments, and the average correlation function was taken (Fig 4d). Flow property interactions were analysed based upon the maximum or minimum correlation coefficients that indicated the co-variation trend. Note the positive maximum correlation coefficient $(R_{yc})_{max}$ exhibited around $\tau = 0$ in Figure 4d.

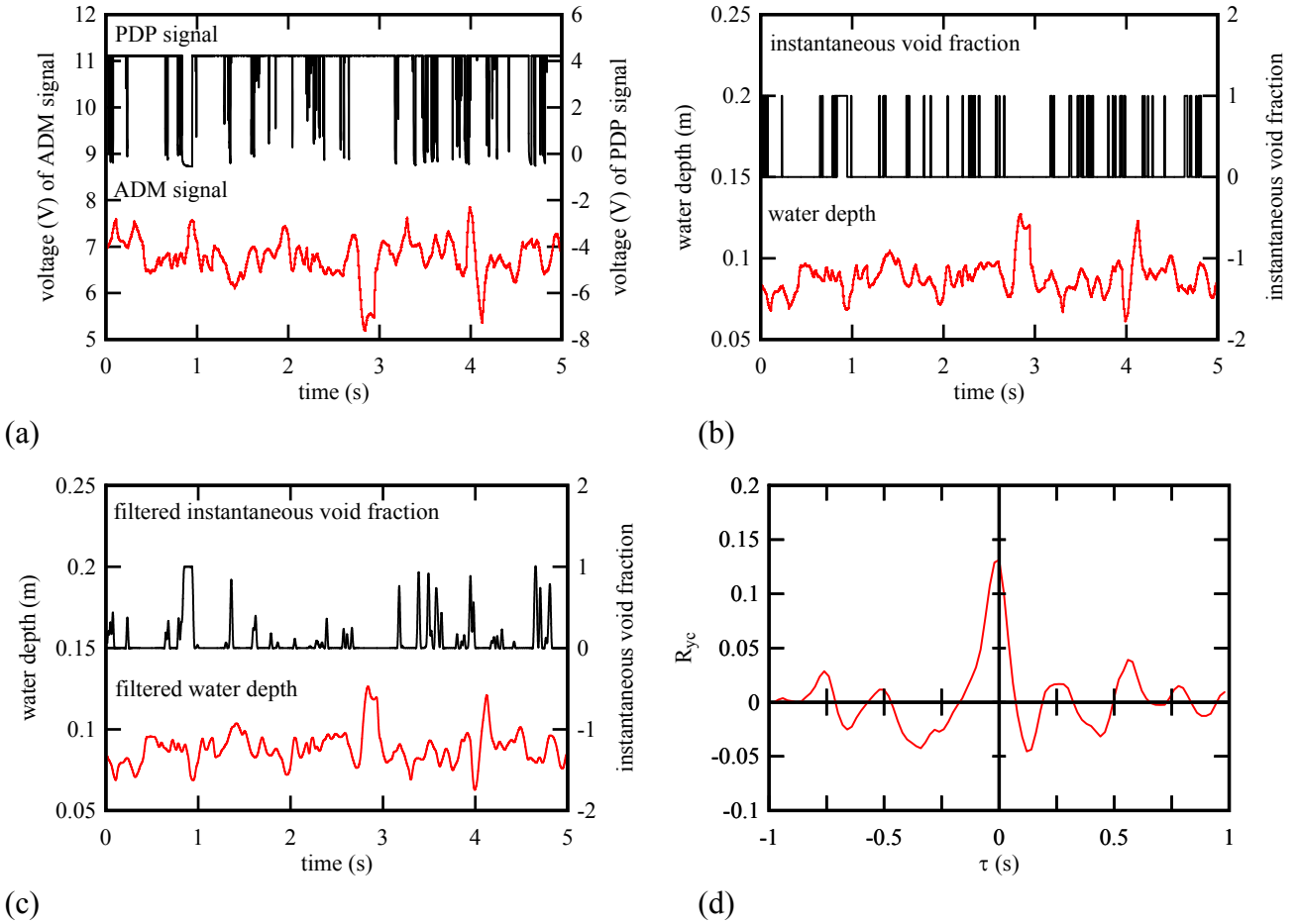

Figure 4. Signal processing for a correlation between water level fluctuation and instantaneous void fraction – Flow conditions: Q = 0.0239 m^3/s, d_1 = 0.0209 m, x_1 = 0.83 m, x-x_1 = 0.167 m, y = 0.056 m, Fr_1 = 5.1, Re = 4.8×10^4. (a) Raw voltage signals of acoustic displacement meter and phase-detection probe (b) Converted water depth and instantaneous void fraction signals (c) Filtered and smoothed signals – filtering cut-off frequency: 50 Hz (d) Averaged cross-correlation function over six 30-s signal segment pairs

2.4 Flow conditions

All experiments were performed with hydraulic jumps with partially-developed inflow conditions. Four inflow Froude numbers (Fr_1 = 3.8, 5.1, 7.5 and 8.5) were applied with identical inflow length x_1/h = 41.5 and intake aspect ratio h/W = 0.04, where x_1 is the longitudinal distance from the upstream gate to the mean jump toe position, h is the gate opening and W is the channel width. The flow conditions are summarised in Table 2.

Table 2. Experimental flow conditions

Test	Q (m^3/s)	W (m)	h (m)	x_1 (m)	d_1 (m)	V_1 (m/s)	Fr_1	Re
1	0.0179	0.5	0.02	0.83	0.0206	1.74	3.8	3.5×10^4
2	0.0239	0.5	0.02	0.83	0.0209	2.29	5.1	4.8×10^4
3	0.0347	0.5	0.02	0.83	0.0206	3.37	7.5	6.8×10^4
4	0.0397	0.5	0.02	0.83	0.0208	3.82	8.5	8.0×10^5

Notes: Q: flow rate; W: channel width; h: upstream gate opening; x_1: longitudinal jump toe position; d_1: inflow depth; V_1: average inflow velocity; Fr_1: inflow Froude number; Re: inflow Reynolds number.

3 Basic results

3.1 Free-surface fluctuations and jump toe oscillations

The instantaneous water level above the jump roller was measured along the channel centreline. The time-averaged free-surface profile was derived, and its fluctuation amplitude was characterised by the water depth standard deviation. The results are presented in Figure 5a with the error bars indicating the characteristic fluctuation amplitude. The higher downstream water level for a larger Froude number was well predicted by momentum conservation (Bélanger 1841). The water depth fluctuations were observed to be maximum close to the jump toe, enhanced with increasing Froude number and decayed at downstream of the roller. The free-surface measurements covered the whole roller length for Tests 1, 2 and 3 (Table 2), where the roller length L_r is defined as the longitudinal distance over which the mean water level increases monotonically (Murzyn et al. 2007). The roller length data derived from the mean free-surface profiles were consistent with most previous studies. A simple correlation was given based upon a number of studies including the present study, Murzyn et al. (2007), Kucukali & Chanson (2008), Murzyn & Chanson (2009) and Wang & Chanson (2014):

$$\frac{L_r}{d_1} = 6 \times (Fr_1 - 1) \qquad \text{for } 2 < Fr_1 < 10 \quad (1)$$

where d_1 is the inflow depth.

The longitudinal jump toe oscillations were detected by the upstream sensor. The oscillation amplitude, represented by the standard deviation of jump front position, was quantitatively comparable to the inflow depth d_1. The amplitude increased from $0.8 \times d_1$ to $1.5 \times d_1$ for Froude numbers from 3.8 to 8.5. The results were lower than the video data of Zhang et al. (2013) showing the standard deviation of instantaneous impingement point position between d_1 and $2 \times d_1$ on the channel centreline for $3.5 < Fr_1 < 6$. The difference was related to the (herein) higher position of the detected jump front ($y - d_1 \approx 0.03$ m) than the real jump toe ($y = d_1$).

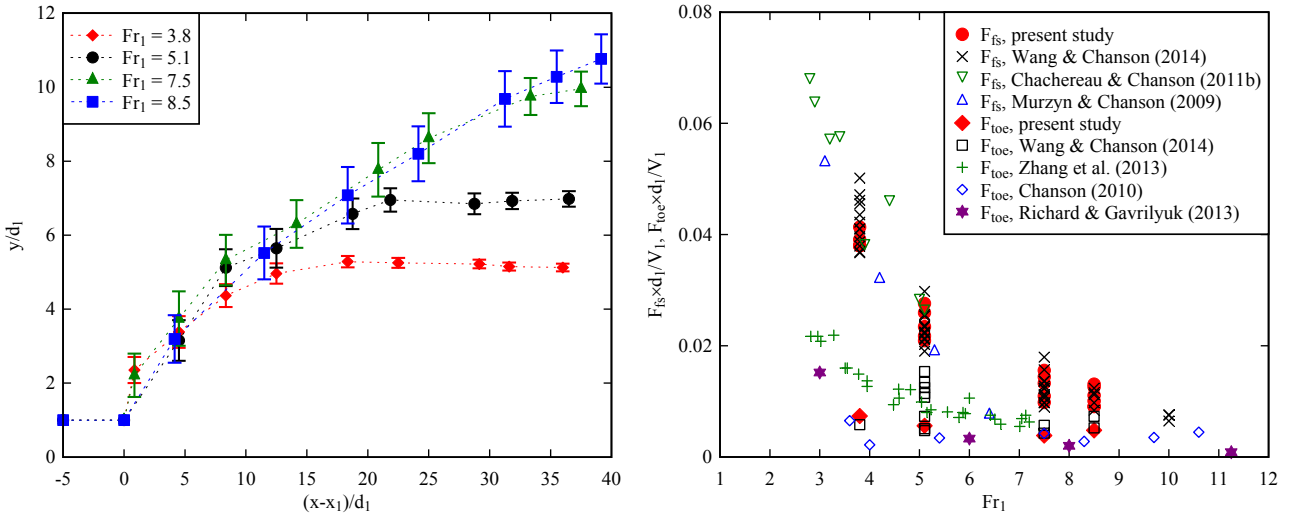

(a) (b)

Figure 5. Fluctuating free-surface motions along the channel centreline. (a, left) Time-averaged free-surface profile and characteristic fluctuation amplitude (b, right) Characteristic frequencies of free-surface fluctuations and longitudinal jump toe oscillations as functions of the Froude number

The characteristic frequencies of the vertical free-surface fluctuations F_{fs} and longitudinal jump toe oscillations F_{toe} were derived from spectral analysis of the ADM signals. Figure 5b presents the dimensionless frequencies, $F_{fs} \times d_1/V_1$ and $F_{toe} \times d_1/V_1$, as functions of the Froude number. The free-surface fluctuations showed higher frequencies than the jump toe oscillation ($F_{fs} > F_{toe}$), and both dimensionless frequencies decreased with increasing Froude number. For each Froude number, a range of free-surface fluctuation frequencies were seen corresponding to different longitudinal positions, slightly higher close to the toe and lower at downstream. The results compared well with the data of Murzyn & Chanson (2009), Chachereau & Chanson (2011b) and Wang & Chanson (2014) with similar instrumentation, of Chanson (2010) and Zhang et al. (2013) with visual observations, and of Richard & Gavrilyuk (2013) with numerical computation.

3.2 Air-water flow properties

As the upstream flow impinged into the jump roller, a turbulent shear layer formed in the lower part of the roller with air entrapped at the impingement point, while the upper roller was characterised by flow recirculation and free-surface aeration (Fig 2). The phase-detection probe measured the time-averaged void fraction C ($C = \overline{c}$) at a given location. The vertical void fraction distributions for Test 3 are shown in Figure 6a at different longitudinal positions. The void fraction profiles showed different shapes in the two flow regions: the bell-shape distribution in the turbulent shear region, as well as its longitudinal variation, was associated with the advection and diffusion of the air bubbles entrained at the jump toe; the rapidly increasing void fraction in the free-surface region reflected the interfacial aeration. The boundary between the turbulent shear region and free-surface region was identified at the elevation of local minimum void fraction $y = y^*$. The upper boundary of the free-surface region was considered at the characteristic elevation $y = Y_{90}$ where the time-averaged void fraction $C = 0.9$ (Cain & Wood 1981). Note that Y_{90} was above the mean water elevation detected by the displacement meters.

The frequency of air-water interface detection was linked to the bubble count rate. Figure 6b presents the vertical distributions of dimensionless bubble count rate $F \times d_1/V_1$ for Test 3. The bimodal profile exhibited a marked maximum in the turbulent shear region ($0 < y < y^*$) and a secondary peak next to the free-surface ($y^* < y < Y_{90}$). Both peak values decreased with increasing distance from the jump toe. The vertical position of the maximum bubble count rate was beneath the local maximum void fraction in the shear region (Fig 6a), indicating the non-coincidence between the maximum air advection layer and maximum turbulent shear layer. The magnitude of bubble count rate was highly affected by the Reynolds number hence the turbulence level of the flow. It is noteworthy that the phase-detection probe was scanned at 5 kHz. This relatively low sample rate would lead to an underestimate of bubble count rate when the Reynolds number was high (Wang et al. 2014c).

The time-averaged air-water interfacial velocity was calculated as $V = \Delta x/T$, where Δx is the longitudinal distance between two phase-detection sensor tips and T is the average time of air-water interfaces travelling over the distance Δx. T was deduced from the cross-correlation function between the phase-detection probe signals. Figure 6c shows the vertical distributions of interfacial velocity, highlighting positive average velocity in most part of the shear region and negative velocity in the recirculation region. Such a flow reversal did not occur over the full roller length. A longer recirculation region relative to the roller length was observed at larger Froude numbers. The velocity data was meaningless in the transition area between the shear and free-surface regions, because the correlation method did not provide accurate estimate to the time-averaged characteristics for the flow with frequent change in flow direction (hence mean velocity close to zero). Next to the bottom, a maximum velocity was seen, and it decreased longitudinally as the kinetic energy was dissipated.

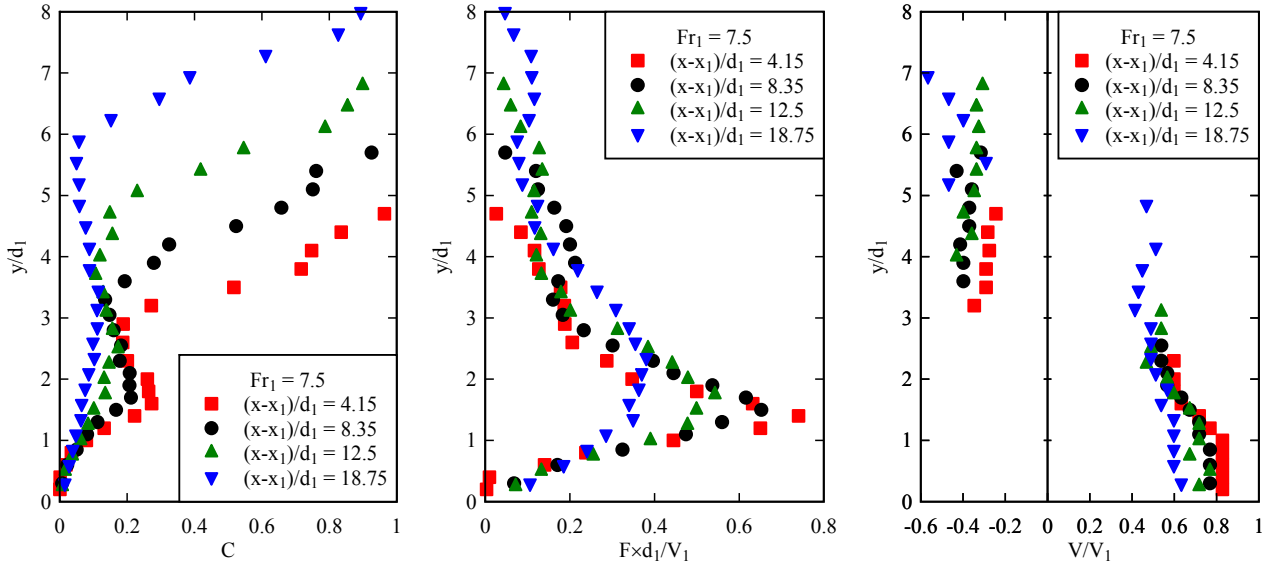

(a) (b) (c)

Figure 6. Vertical distributions of (a, left) time-averaged void fraction, (b, middle) bubble count rate and (c, right) interfacial velocity at different longitudinal positions for Test 3

3.3 Total pressure in turbulent shear flow region

Figure 7a presents the vertical distributions of dimensionless mean total pressure $P/(0.5\times\rho\times V_1^2)$ measured with the total pressure probe, where ρ is the water density. The data are shown in the turbulent shear region where the flow velocity was mostly positive against the probe orientation. In the upper flow region, the presence of reversed flow led to meaningless total pressure probe data. For all tested Froude numbers, the typical mean total pressure profile exhibited a maximum at an elevation between $0.5\times d_1$ and $0.9\times d_1$, close to the elevation of maximum velocity. The maximum total pressure decreased with increasing distance from the jump toe as the velocity hence kinetic pressure decreased.

The total pressure fluctuations were characterised by the standard deviation of the instantaneous total pressure. The vertical distributions in the turbulent shear region are shown in Figure 7b for the given flow conditions. A marked maximum was shown, corresponding to the occurrence of maximum total pressure fluctuations. The maximum fluctuation amplitude decreased along the roller, as the free-surface fluctuations and the velocity turbulence were milder at downstream of the roller. The vertical position of the maximum total pressure fluctuation was higher than that of the maximum mean total pressure (Fig 7a), and typically lower than the elevation of maximum bubble count rate (Fig 6b). At a given longitudinal position, the dimensionless total pressure fluctuation increased with an increasing Froude number.

The side-by-side mounted phase-detection probe and total pressure probe allowed for a direct comparison between the measured total pressure and the expected value calculated as:

$$P(y) = \int_{y}^{Y_{90}} (1-C)\times\rho\times g\times dy + \frac{1}{2}\times(1-C)\times\rho\times V^2 \quad (2)$$

where ρ is the water density. In a high-speed bubbly flow such as hydraulic jump, the flow velocity and air-water interfacial velocity is considered equivalent (i.e. no slip). The first term on the right

hand side of Equation (2) is the piezometric pressure P_o and the second item is the kinetic pressure P_k. A comparison between the experimental data and the calculation results of Equation (2) is shown in Figure 7c. The reasonable agreement validated the application of such total pressure transducer in the highly turbulent and aerated flow. Further the piezometric pressure distribution derived from the void fraction measurements indicated that the jump roller was hydrostatic taking into account the flow aeration, i.e. $\partial P_o/\partial y = -(1-C)\times\rho\times g$.

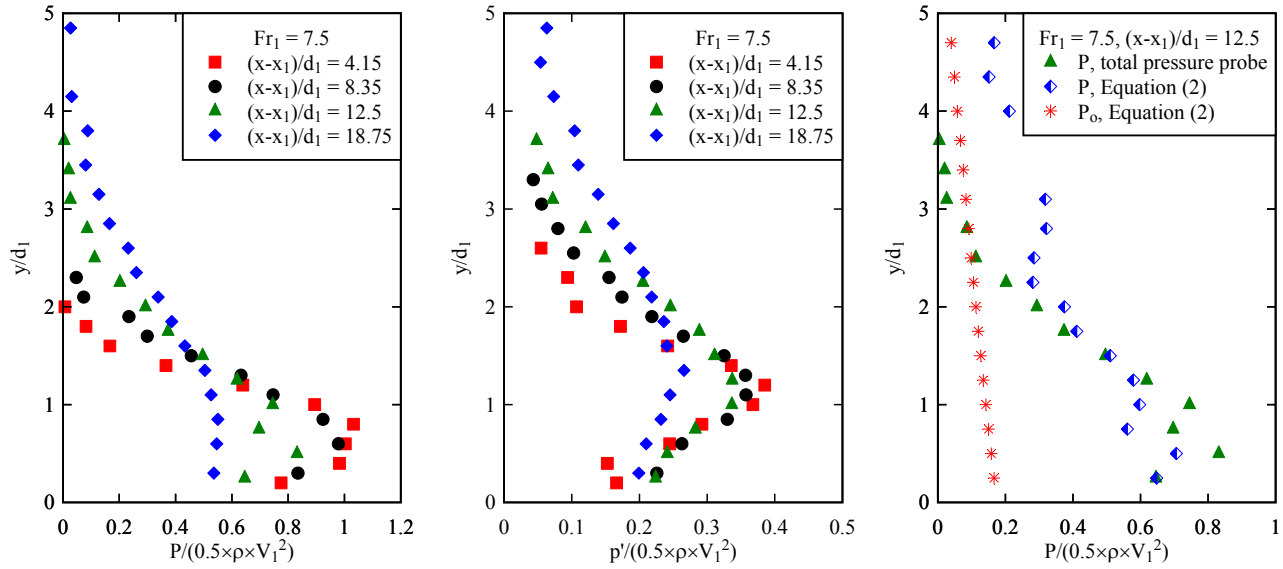

(a) (b) (c)

Figure 7. Total pressure and fluctuations in the turbulent shear region for Test 3: (a, left) Mean total pressure distributions (b, middle) Total pressure fluctuations (c, right) Comparison between experimental and theoretical mean total pressures, together with piezometric pressure distribution

4 Correlation between free-surface deformation, air entrainment and total pressure fluctuation

4.1 Two-dimensional free-surface deformation

The instantaneous horizontal jump front position was correlated with the simultaneously recorded water elevations at different longitudinal positions along the channel centreline. The sign of cross-correlation function maximum/minimum around zero time lag reflected a trend of simultaneous variation between the two motions. The maximum/minimum correlation coefficients $(R_{xy})_{max}$ are plotted in Figure 8 as a function of the relative longitudinal position $(x-x_1)/L_r$ where the water elevation was measured. With x positive in the downstream direction and y positive in the upward direction, a positive correlation indicated that the local free-surface moved upwards when the jump front moved downstream, and vice versa. Conversely a negative (minimum) coefficient indicated that the water surface elevation decreased when the jump toe travelled downstream. The data showed negative minimum correlations in the first half of the roller ($(x-x_1)/L_r$ < 0.4 to 0.5), and positive maximum correlations in the second half roller ($(x-x_1)/L_r$ > 0.4 to 0.5). The data are compared with Wang & Chanson (2014) for Fr_1 = 5.1 with a range of Reynolds numbers from 2.1×10^4 to 1.6×10^5. The average distribution trend is marked in dashed. The results revealed an average two-dimensional roller surface deformation pattern, as sketched in Figure 9. That is, the rapid jump toe oscillations were linked with a deformation of the roller surface rather than a simple translation of the jump. Note that the sketched free-surface motions in Figure 9 were some flow patterns with the largest possibility of occurrence. Other instantaneous surface deformation patterns might also exist (see below).

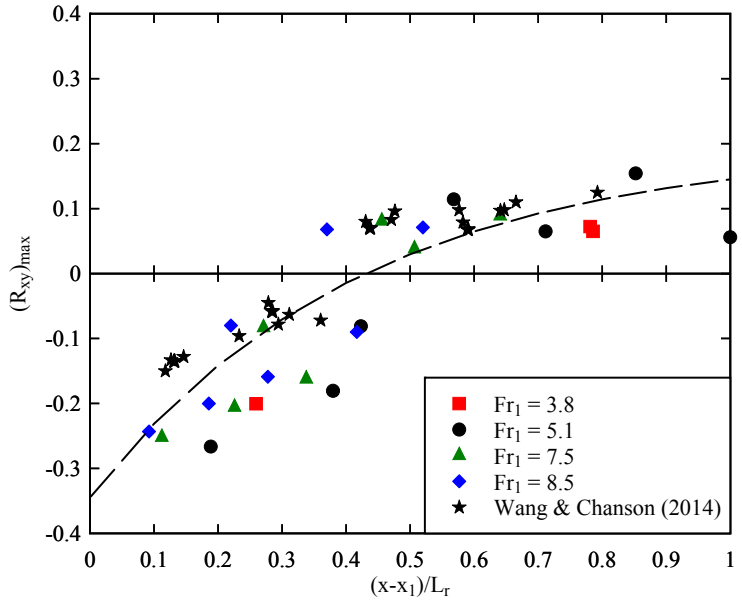

Figure 8. Longitudinal distributions of maximum correlation coefficient $(R_{xy})_{max}$ between horizontal and vertical roller free-surface motions within the jump roller length – Comparison with data of Wang & Chanson (2014) for $Fr_1 = 5.1$, $2.1\times10^4 < Re < 1.6\times10^5$

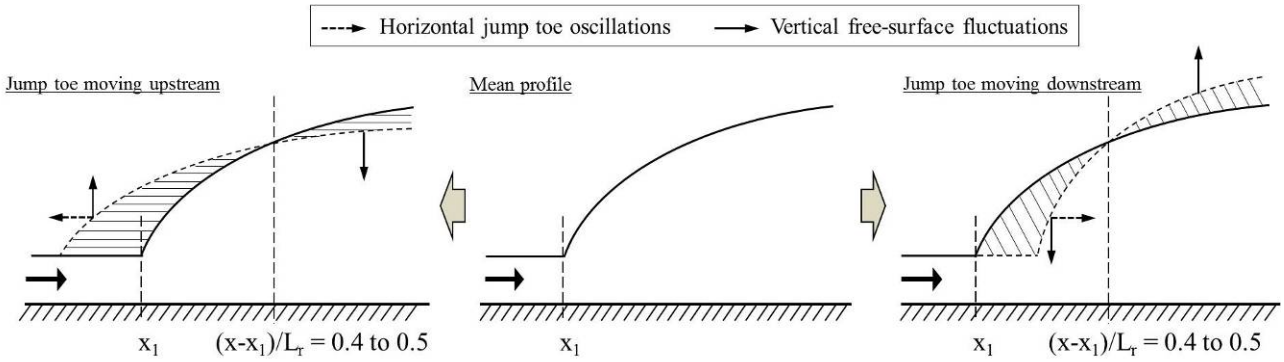

Figure 9. Sketches of the average roller surface deformation pattern deduced from correlation analysis between the horizontal and vertical surface motions

4.2 Free-surface motions and air entrainment

The correlation between the signals of horizontal acoustic displacement meter and phase-detection probe provided a measure of the simultaneous variation in longitudinal jump toe oscillation and local air content at the phase-detection sensor position. Similarly the simultaneous variation in vertical free-surface fluctuation and local air content were characterised by correlation between the signals of phase-detection probe and displacement meter above. The corresponding cross-correlation functions R_{xc} and R_{yc} showed different characteristic shapes between the turbulent shear region and free-surface region. A typical correlation function R_{yc} in the shear region can be seen in Figure 4d. The positive maximum correlation coefficient $(R_{yc})_{max} > 0$ indicated an instantaneous increase in water level with increasing void fraction underneath at $y/d_1 = 2.8$ (Fig. 4d). The maximum correlation coefficients $(R_{xc})_{max}$ and $(R_{yc})_{max}$ were analysed in several cross-sections, and their typical vertical distributions are plotted in Figure 10a for $Fr_1 = 5.1$ at $(x-x_1)/d_1 = 4.2$ and in Figure 10b for $Fr_1 = 8.5$ at $(x-x_1)/d_1 = 8.4$, both in the first half of the roller. The time-averaged void fraction C is also shown for comparison. In Figure 10a, the data are compared with those of Wang & Chanson (2014) for the same flow conditions, the consistency indicating the repeatability of the measurements and analysis.

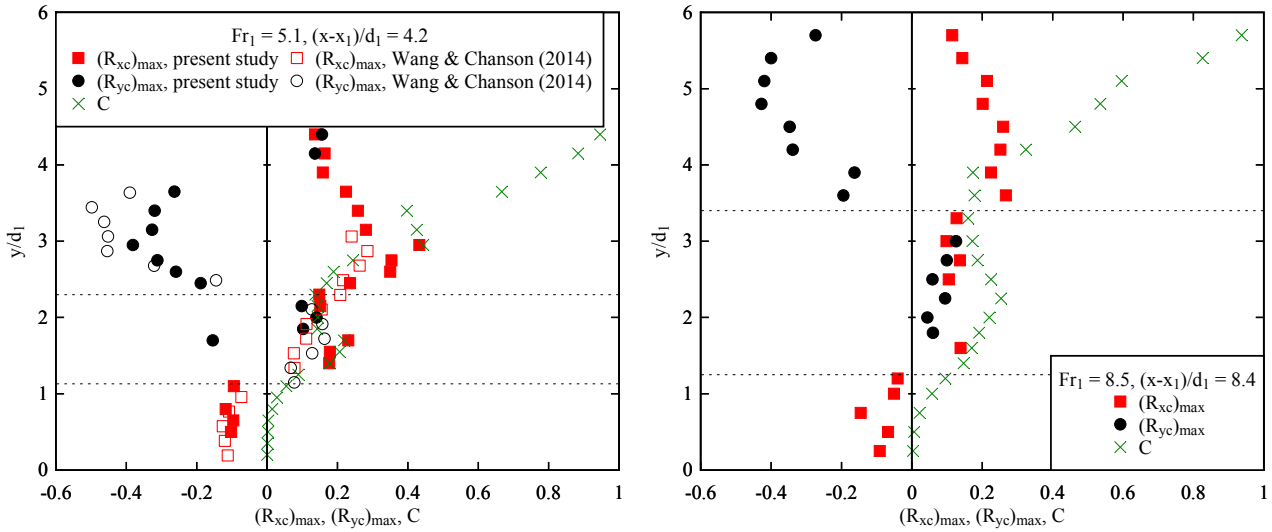

Figure 10. Vertical distributions of maximum correlation coefficients between roller surface deformation and instantaneous void fraction – Comparison with time-averaged void fraction. (a, left) Test 2, $(x\text{-}x_1)/d_1 = 4.2$ (b, right) Test 4, $(x\text{-}x_1)/d_1 = 8.4$

In the first half of the roller, the vertical distributions of $(R_{xc})_{max}$ and $(R_{yc})_{max}$ exhibited different shapes in three flow regions from bottom to free-surface. First, in the lower turbulent shear region where the time-averaged void fraction was small, the correlation R_{yc} did not show unique maximum, while the maximum correlation coefficient $(R_{xc})_{max}$ was negative. It meant that the local void fraction decreased when the jump toe moved downstream, and was almost independent of the free-surface fluctuations. Note that the void fraction signal was filtered at 50 Hz, thus an increase in instantaneous void fraction hardly reflected the arrival of individual bubbles but more likely of an amount of entrapped air, e.g. some bubble clusters or air pockets. At a fixed longitudinal position close to the toe, the downstream movement of jump toe reduced the local air content in the lower shear region because the relative distance to the toe decreased and the location of phase-detection probe sensor was then beneath the convective shear layer. Second, in the main shear layer where the time-averaged void fraction was about the local maximum, both correlation functions showed positive maxima. i.e. $(R_{xc})_{max} > 0$ and $(R_{yc})_{max} > 0$. It implied that, when the instantaneous void fraction increased, the jump toe moved downstream and the free surface elevation above the phase-detection probe sensor shifted upwards. Such behaviour could correspond to the formation and detachment of large highly-aerated vortices from the jump toe and the associated flow bulking. Third, in the upper recirculation region, $(R_{xc})_{max}$ was positive and $(R_{yc})_{max}$ became negative, corresponding to a downstream movement of jump toe, drop in free surface level and local increase in void fraction. This could derive from some roller surface deformation instantaneously placing the phase-detection probe sensor closer to the free-surface in a region of higher void fraction. Note that the increase in water level caused by flow bulking was inconsistent with the simultaneous decrease of water level when the jump toe moved downstream, as given in Figure 9. This was because both trends were shown as statistical results and they did not necessarily occur at the same moment. The roller surface deformation pattern revealed by the correlation R_{xy} (Fig. 9) suggested that the free-surface lowering with downstream toe motion was detected more frequently.

Further downstream in the second half of the roller, the correlation between the jump toe motion and local air concentration became weak, while the variation of void fraction with water level remained

consistent with that close to the jump toe, i.e. $(R_{yc})_{max} > 0$ for $y < y^*$ and $(R_{yc})_{max} < 0$ for $y > y^*$. The pattern was consistently observed in the air-water region of the roller, thus reflecting the flow bulking in the shear layer with the advection of large amount of air, which was consistent with the free-surface deformation sketched in Figure 9 for $(x\text{-}x_1)/L_r > 0.5$.

The local variation in instantaneous void fraction c with the longitudinal jump toe oscillation and vertical water level fluctuation is sketched in Figure 11 for different parts of the roller. Similar results were observed for all tests with different Froude numbers.

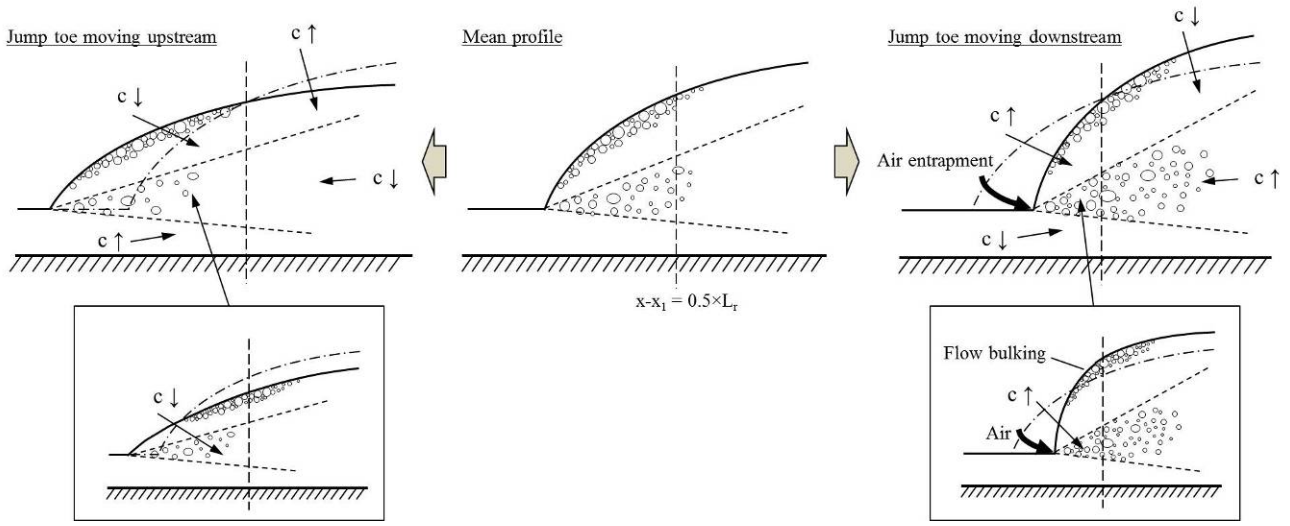

Figure 11. Sketch of simultaneous variations in longitudinal jump toe position, water elevation and void fraction in different parts of jump roller – Arrows indicate the position of phase-detection probe sensor. The bottom figures show patterns less commonly observed in terms of free-surface deformation but typical when correlated with air entrainment

4.3 Free-surface motions and total pressure

The total pressure was coupled with the flow velocity, water depth and void fraction distribution (Eq. (2)). The correlation between the roller surface motions and instantaneous total pressure, R_{xp} and R_{yp}, were investigated in the turbulent shear region ($0 < y < y^*$). Figure 12 presents the maximum correlation coefficients $(R_{xp})_{max}$ and $(R_{yp})_{max}$ at different vertical positions for $Fr_1 = 7.5$. The data distributions highlighted two sub-regions in the shear flow. Figure 12a shows the data in the first half roller, with $(R_{xp})_{max} < 0$ and $(R_{yp})_{max} > 0$ in the main shear layer and $(R_{xp})_{max} > 0$ and $(R_{yp})_{max} < 0$ in the lower shear region below. In the main shear layer, the results implied a decrease in local total pressure with downstream shifting jump toe and decreasing water level. The change in total pressure was likely linked with the change of water depth and associated piezometric pressure fluctuations. In the lower shear region, the results indicated an increase in local total pressure with the same roller surface motions. A downstream shift of jump toe led to an increase in local velocity at the measurement point close to the invert, thus giving a larger kinetic pressure hence total pressure.

Figure 12b presents the distribution of $(R_{xp})_{max}$ and $(R_{yp})_{max}$ in the second half roller. No correlation was shown between the total pressure fluctuation and jump toe oscillation in the main shear layer, while the change in pressure followed changes of water depth hence of piezometric pressure ($(R_{yp})_{max} > 0$). In the lower shear region below, the total pressure fluctuations were mainly affected by the turbulent velocity fluctuations, consistent with the relationship seen close to the jump toe ($(R_{xp})_{max} > 0$). The effects of free-surface fluctuation was almost absent in this region.

Overall the interactions between the roller surface motions and total pressure fluctuations differed between the two sub-regions of the shear flow. The total pressure fluctuations were predominantly affected by the piezometric pressure in the upper shear region and kinetic pressure close to the invert. The variation in total pressure with the motions of jump toe and water level is illustrated in Figure 13. The same results were obtained for different Froude numbers.

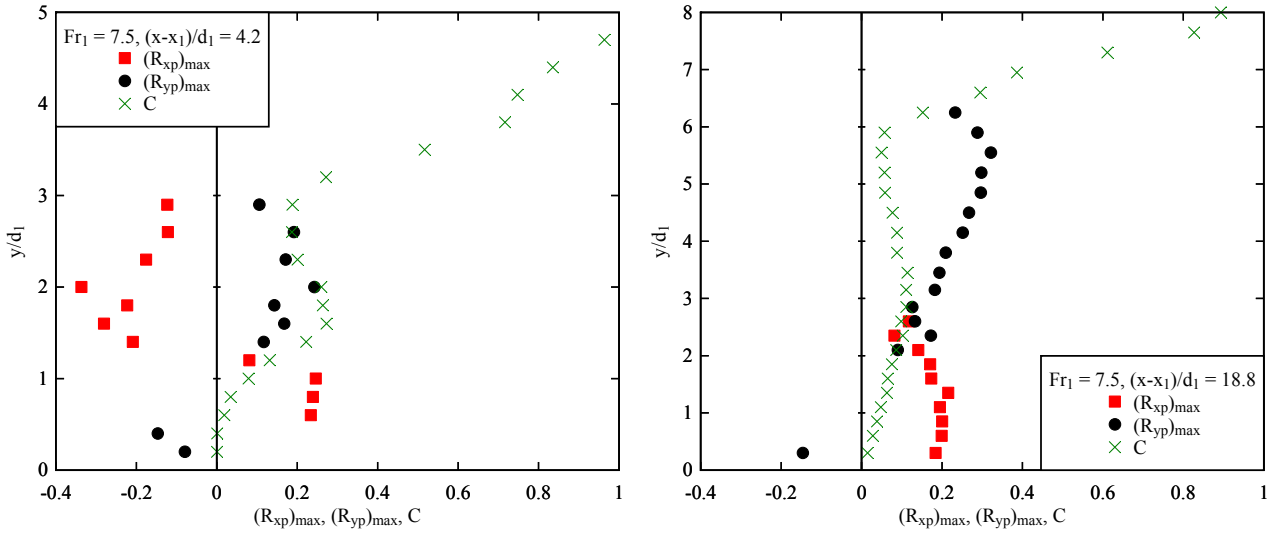

(a) (b)

Figure 12. Vertical distributions of maximum correlation coefficients between roller surface deformation and instantaneous total pressure – Comparison with time-averaged void fraction. (a, left) Test 3, $(x\text{-}x_1)/d_1 = 4.2$ (b, right) Test 3, $(x\text{-}x_1)/d_1 = 18.8$

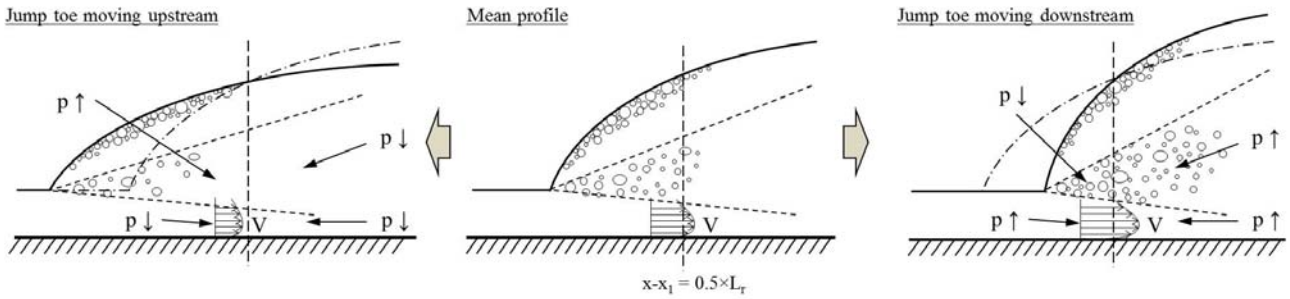

Figure 13. Sketch of simultaneous variations in longitudinal jump toe position, water elevation and total pressure in different parts of turbulent shear region – Arrows indicate the position of total pressure probe sensor

4.4 Air entrainment and total pressure

The interactions between instantaneous total pressure and void fraction were studied based upon filtered signals with an upper cut-off frequency of 2 kHz. Such a cut-off frequency was deemed high enough to cover most known turbulent features of the air-water flow. A typical cross-correlation function R_{pc} showed a distinctive negative minimum with zero time lag in the shear flow. It meant that the instantaneous void fraction increased with a decreasing total pressure. That is, a drop in local total pressure might correspond to the arrival of one or more air bubbles.

A vertical distribution of maximum correlation coefficient $(R_{pc})_{max}$ is plotted in Figure 14 for Fr_1 = 5.1. The data distribution was typical for all flow conditions, showing negative correlation minimum $(R_{pc})_{max} < 0$. The vertical profile of $(R_{pc})_{max}$ exhibited a maximum amplitude between the main and

lower shear regions. In Figure 14, the correlation data are compared with the distributions of time-averaged void fraction and dimensionless pressure fluctuations p'/P_{max}, where P_{max} is the maximum mean total pressure at the cross section. The location of maximum $(R_{pc})_{max}$ and p'/P_{max} were close, suggesting strong correlation between the variation of total pressure and void fraction in the shear flow. The negative correlations between instantaneous void fraction and total pressure could be considered either at a micro-scale or macro-scale level. That is, the increase in void fraction might correspond to the detection of a single air bubble, a bubble cluster or a large-size highly-aerated vortex, and the decrease of total pressure might correspond to either a high-frequency kinetic pressure drop or low-frequency piezometric pressure fluctuation.

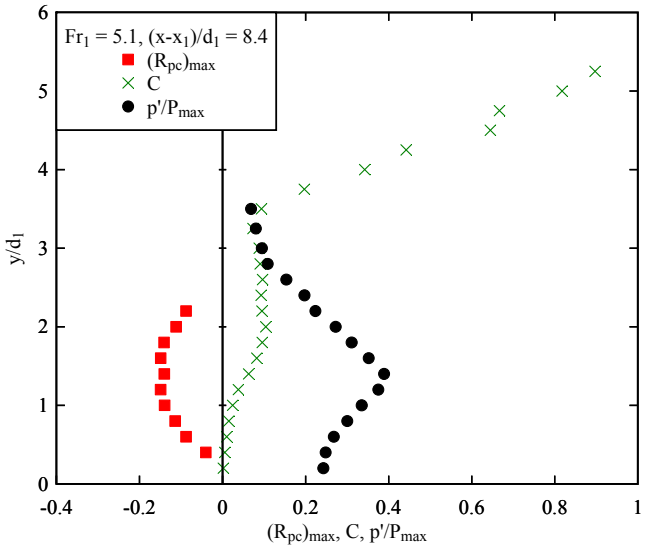

Figure 14. Vertical distributions of maximum correlation coefficients between instantaneous total pressure and void fraction – Comparison with time-averaged void fraction and dimensionless pressure fluctuations p'/P_{max}

4.5 Remarks

Let us consider globally all cross-correlation analyses results between the signals of horizontal jump toe motions, vertical water level fluctuations, instantaneous total pressure and instantaneous void fraction. Table 3 summaries the maximum correlation coefficient signs in different parts of the jump roller, where $y^{\#}$ is the characteristic elevation between the main turbulent shear layer and lower shear region. Some dynamic relationships between the flow properties were revealed. First, in the recirculation region, the instantaneous void fraction was mainly related to the free-surface elevation. When the water level decreased, the void fraction was measured closer to the free surface and increased. Second, in the main turbulent shear layer, the air entrapment process at the impingement point was linked to a downstream shift of jump toe together with flow bulking at the free-surface and an increase in void fraction. The total pressure data suggested a strong link between the water depth variations and piezometric pressure fluctuations. Third, in the lower shear region next to the invert, the void fraction and total pressure were both related to the relative position to the toe, which determined the development of the convective air-water shear layer. A downstream jump toe motion led to a decreasing void fraction and an increasing total pressure. The kinetic pressure fluctuations were the dominant component to the total pressure fluctuations in the lower shear flow.

Table 3. Summary of maximum correlation coefficient signs in different part of hydraulic jump roller

Flow region		$(R_{xy})_{max}$	$(R_{xc})_{max}$	$(R_{yc})_{max}$	$(R_{xp})_{max}$	$(R_{yp})_{max}$	$(R_{pc})_{max}$
$0 < (x\text{-}x_1)/L_r < 0.5$,	$y^* < y < Y_{90}$	-	+	-	N/A	N/A	N/A
$0 < (x\text{-}x_1)/L_r < 0.5$,	$y^{\#} < y < y^*$	-	+	+	-	+	-
$0 < (x\text{-}x_1)/L_r < 0.5$,	$0 < y < y^{\#}$	-	-	N/A	+	-	-
$0.5 < (x\text{-}x_1)/L_r < 1$,	$y^* < y < Y_{90}$	+	N/A	-	N/A	N/A	N/A
$0.5 < (x\text{-}x_1)/L_r < 1$,	$y^{\#} < y < y^*$	+	N/A	+	+	+	-
$0.5 < (x\text{-}x_1)/L_r < 1$,	$0 < y < y^{\#}$	+	N/A	N/A	+	-	-

Notes: L_r: jump roller length; Y_{90}: upper boundary of free-surface region with C = 0.9; y^*: boundary between free-surface region and turbulent shear layer; $y^{\#}$: boundary between main and lower shear region; N/A: not available.

5 Discussion

The jump roller is traditionally divided into two main flow regions, i.e. the turbulent shear region next to the bottom and the recirculation region above, according to the distributions of time-averaged air-water flow properties (Murzyn & Chanson 2009). In the shear region, the flow properties are largely controlled by the turbulence field, while the gravity force plays a major role in the recirculation region.

The turbulent shear region is characterised by a convective transport of air bubbles entrapped at the jump toe and advected downstream in large vortical structures (Hoyt & Sellin 1989). The bubbly flow is further affected by de-aeration caused by buoyancy effects. These processes are illustrated by the vertical distributions of the time-averaged void fraction (Fig 15). Figure 15 shows a typical series of void fraction profiles along the hydraulic jump roller. The boundary between the recirculation region and shear layer is highlighted with a dotted and dashed line. In the shear region, the void fraction profiles showed a broadening of the bell-shape with increasing distance from the jump toe, as the local maximum void fraction decreased. This region of relatively high void fraction outlined the preferential path of large highly-aerated vortices. It is termed the main shear layer herein and sketched in Figure 15 between two characteristic vertical positions $y^{\#}$ and y^*. The lower shear region ($y < y^{\#}$) is sketched in Figure 15 beneath the dashed line. It is a thin layer where the boundary friction is important and the void fraction is small.

The distinction between the two sub-regions, main shear layer and lower shear region, was clearly seen in terms of coupling between instantaneous total pressure, void fraction and roller surface locations. The major differences were two-fold. First the main shear layer was a highly-aerated region, while the air content in the lower shear region was very small. In the main shear layer, air was convected in large vortical structures which evolved and enlarged with time through vortex pairing in a manner similar to the observations of Brown & Roshko (1974). The thickness of the main shear layer increased rapidly along the roller (Fig 15). The vortex path rose with increasing distance because of a combination of buoyancy and interactions between vortices and the invert. The air bubbles diffused across the shear region during their convection, with the total air content and the maximum void fraction decreasing in the longitudinal direction. In the lower shear layer, the effects of the invert included boundary friction (no-slip condition) and a symmetry line by analogy with two-dimensional plunging jets (Cummings & Chanson 1997). Only a small number of air bubbles diffused in the vicinity of the solid boundary. The thickness of the lower shear layer decreased with increasing distance from the jump toe as illustrated in Figure 15. Second the main shear layer was the locus of large velocity shear and velocity fluctuations (i.e. high turbulence intensity), while the lower shear region tended to experience lower turbulence levels. On the one hand, the time-averaged

velocity reached a maximum close to the bottom then decreased with increasing elevation till negative in the recirculation region. On the other hand, the turbulence intensity presented a monotonic increasing trend with increasing elevation through the shear layer (Wang et al. 2014a). The higher turbulent level in the main shear layer was linked to a number of phenomena, including the pseudo-periodic vortex formation, the longitudinal jump toe oscillations and turbulence modulation by entrained air. The lower shear region was less affected by the large-scale turbulent structures and the velocity field was comparatively more organised than in the main shear layer. This was in accordance with the flow visualisations as well.

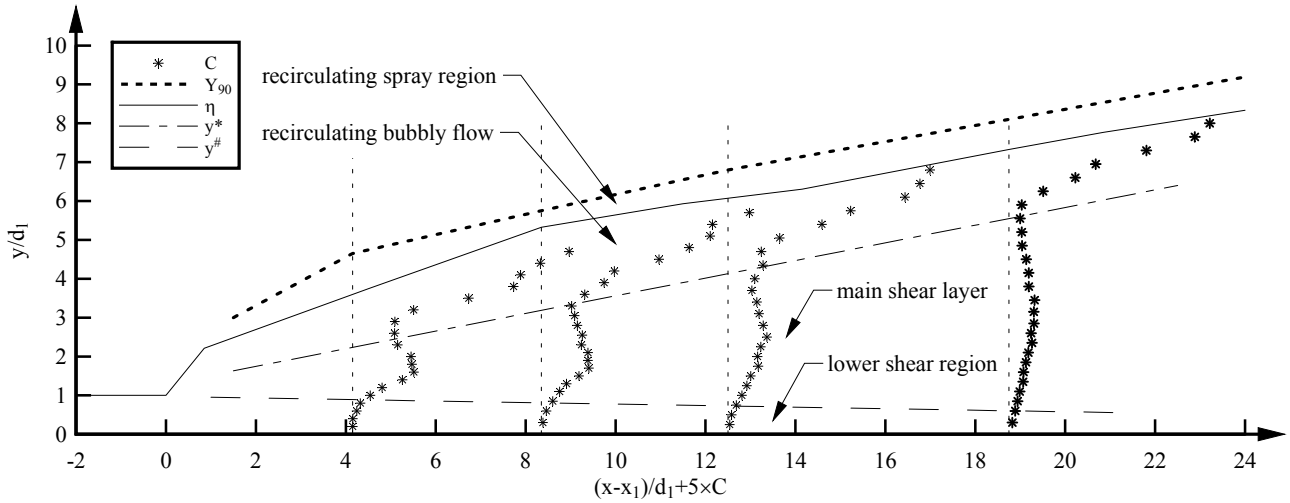

Figure 15. Longitudinal development of void fraction profiles and sketch of the sub-regions in the turbulent shear region for Test 3

The boundary between the main and lower shear regions was not strictly defined, for example, as a function of local void fraction. Nevertheless, the vertical distributions of maximum correlation coefficients provided the means to estimate of the boundary positions. Figure 16 presents the estimation results as the relative positions in the shear layer, where $y^{\#}$ denotes the boundary between the two sub-regions of shear layer and y^* is the characteristic elevation of the boundary between shear layer and recirculation region. In Figure 16, the mean free-surface profile is also shown in terms of η and Y_{90}, where η is the time-averaged water elevations measured with the acoustic displacement meters and Y_{90} is the elevation with $C = 0.9$. The region between y^* and η is considered as the recirculating bubbly flow and that between η and Y_{90} the spray and splashing area above roller. All data sets presented some self-similar trends, best fitted by:

$$\frac{y^{\#} - d_1}{d_2 - d_1} = 0.0217 \times \frac{x - x_1}{L_r} \qquad r = 0.9903 \quad (3)$$

$$\frac{y^* - d_1}{d_2 - d_1} = 0.122 + 0.714 \times \frac{x - x_1}{L_r} \qquad r = 0.9696 \quad (4)$$

$$\frac{\eta - d_1}{d_2 - d_1} = \left(\frac{x - x_1}{L_r} \right)^{0.537} \qquad r = 0.9839 \quad (5)$$

$$\frac{Y_{90} - d_1}{d_2 - d_1} = 1.1 \times \left(\frac{x - x_1}{L_r} \right)^{0.413} \qquad r = 0.9151 \quad (6)$$

where d_2 is the conjugate flow depth and r is the normalised correlation coefficient. Equation (3) suggested an almost constant thickness of the lower shear region: $y^{\#} \approx d_1$.

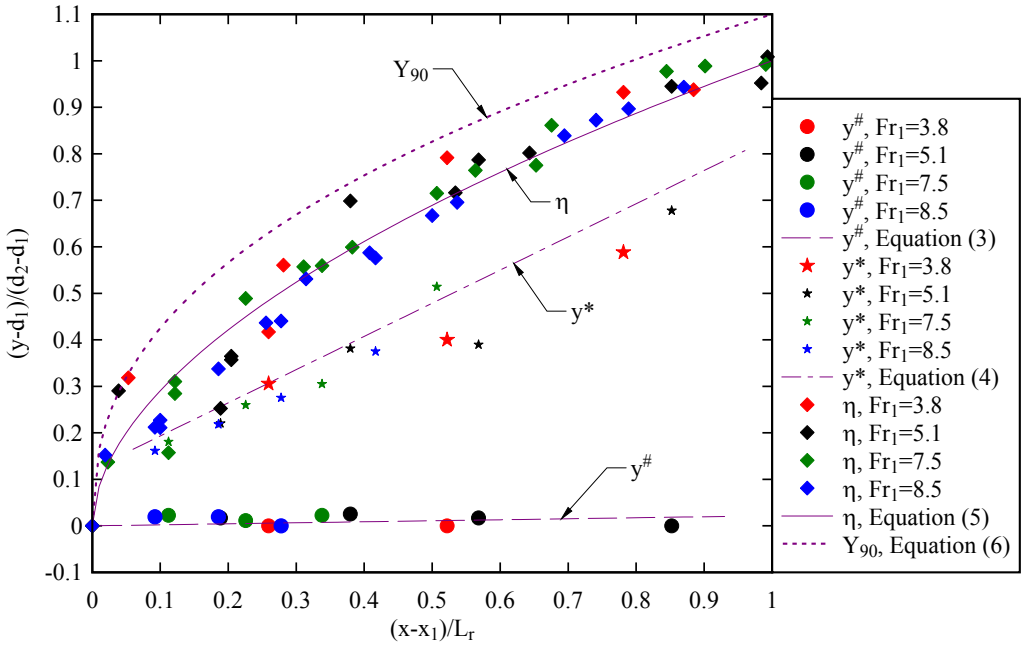

Figure 16. Self-similar flow structures in jump roller: characteristic thickness of main shear layer and lower shear sub-regions

6 Conclusion

Fluctuations in toe position, water level, air content and total pressure were measured simultaneously in hydraulic jumps for Froude numbers from 3.8 to 8.5. The mean profile, fluctuation amplitude and frequencies of the roller surface were analysed. Detection of air-water interfaces provided void fraction, bubble count rate and interfacial velocity distributions. The total pressure was measured with a miniature pressure transducer in the positive velocity flow region. The experimental results compared well with the theoretical values calculated by void fraction, water depth and interfacial velocity. The prediction of two-phase flow measurements also indicated a time-averaged hydrostatic flow in the jump roller, though the large-scale flow turbulence was inhomogeneous and nonisotropic. The mean total pressure reached maximum in the lower part of shear flow, close to the position of maximum velocity, while the maximum total pressure fluctuation was observed at a slightly higher elevation. Both mean and fluctuation decreased with increasing longitudinal distance and with increasing Froude number.

The interactions between the free-surface deformation, air entrainment and total pressure fluctuations were investigated with cross-correlation of the corresponding signals. Some common free-surface deformation patterns were revealed, which interacted with the variation of instantaneous void fraction and total pressure in different parts of the roller. The longitudinal jump toe oscillation affected the extent of deceleration and aeration of the lower shear flow next to the invert. It also associated with the air entrapment at the jump toe. The water level fluctuation reflected both flow bulking and surface deformation linked to the jump toe oscillation. The change of total pressure

followed respectively the change in water level and flow velocity in the main shear layer and lower shear region. The different characteristics of the main shear layer and lower shear region were discussed at the end.

Acknowledgements
The financial supports of the Australian Research Council (DP120100481), The University of Queensland, and ESTACA (France) are acknowledged.

References

Abdul Khader MH, Elango K (1974) Turbulent pressure field beneath a hydraulic jump. Journal of Hydraulic Research 12(4):469-489

Babb AF, Aus HC (1981) Measurements of air in flowing water. Journal of Hydraulic Division, ASCE 107(HY12):1615-1630

Bélanger JB (1841) Notes sur l'hydraulique. (Notes on hydraulic engineering.) Ecole Royale des Ponts et Chaussées, Paris, France, session 1841-1842, 223 pages (in French)

Bidone G (1819) Le remou et sur la propagation des ondes. (The jump and on the wave propagation.) Report to Académie Royale des Sciences de Turin, séance 12 Dec., XXV:21-112 (in French)

Bowers CE, Toso JW (1988) Karnafuli project, model studies of spillway damage. Journal of Hydraulic Engineering 114(5):469-483

Brown GL, Roshko A (1974) On density effects and large structure in turbulent mixing layers. Journal of Fluid Mechanics 64(4):775-816

Cain P, Wood IR (1981) Measurements of self-aerated flow on spillways. Journal of Hydraulic Division, ASCE 107(HY11):1425-1444

Chachereau Y, Chanson H (2011a) Bubbly flow measurements in hydraulic jumps with small inflow Froude numbers. International Journal of Multiphase Flow 37(6):555-564

Chachereau Y, Chanson H (2011b) Free-surface fluctuations and turbulence in hydraulic jumps. Exp Thermal Fluid Sci 35(6):896–909

Chanson H (1995) Air entrainment in two-dimensional turbulent shear flows with partially developed inflow conditions. International Journal of Multiphase Flow 21(6):1107-1121

Chanson H (2007) Bubbly flow structure in hydraulic jump. European Journal of Mechanics B/Fluids 26(3):367-384

Chanson H (2010) Convective transport of air bubbles in strong hydraulic jumps. International Journal of Multiphase Flow 36(10):798-814. doi:10.1016/j.ijmultiphaseflow.2010.05.006

Chanson H, Brattberg T (2000) Experimental study of the air-water shear flow in a hydraulic jump. International Journal of Multiphase Flow 26(4):583-607

Cox D, Shin S (2003) Laboratory measurements of void fraction and turbulence in the bore region of surf zone waves. J. Eng. Mech. 129(10):1197-1205

Cummings PD, Chanson H (1997) Air entrainment in the developing flow region of plunging jets – part 1: theoretical development. Journal of Fluids Engineering, Transactions ASME 199:597-602

Farhoudi J, Narayanan R (1991) Force on slab beneath hydraulic jump. Journal of Hydraulic Engineering 117(1):64-82

Fiorotto V, Rinaldo A (1992) Fluctuating uplift and lining design in spillway stilling basins. Journal of Hydraulic Engineering 118(4):578–596

Hager WH (1992) Energy Dissipators and Hydraulic Jump. Kluwer Academic Publishers, Water Science and Technology Library, Vol. 8, Dordrecht, the Netherlands, 288 pages

Hoyt JW, Sellin RHJ (1989) Hydraulic jump as 'mixing layer'. Journal of Hydraulic Engineering 40(3):1607-1614

Kucukali S, Chanson H (2008) Turbulence measurements in the bubbly flow region in hydraulic jumps. Experimental Thermal and Fluid Science 33(1):41-53

Lighthill J (1978) Waves in fluids. Cambridge University Press, Cambridge, UK

Long D, Rajaratnam N, Steffler PM, Smy PR (1991) Structure of flow in hydraulic jumps. Journal of Hydraulic Research, IAHR 29(2):207-218

Longo S (2010) Experiments on turbulence beneath a free-surface in a stationary field generated by a Crump weir: free-surface characteristics and the relevant scales. Experiments in Fluids, 49:1325-1338

Lopardo RA (2013) Extreme velocity fluctuations below free hydraulic jumps. Journal of Engineering, Hindawi Publishing Corporation, Article ID 678065

Lopardo RA, Henning RE (1985) Experimental advances on pressure fluctuations beneath hydraulic jumps. Proceedings of 21st IAHR Biennial Congress, Melbourne, Australia, pp. 633-637

Montes JS (1998) Hydraulics of Open Channel Flow. ASCE Press, New York, USA

Mouaze D, Murzyn F, Chaplin JR (2005) Free surface length scale estimation in hydraulic jumps. Journal of Fluids Engineering, Transactions ASME 127:1191-1193

Murzyn F, Mouaze D, Chaplin JR (2005) Optical fibre probe measurements of bubbly flow in hydraulic jumps. International Journal of Multiphase Flow 31(1):141-154

Murzyn F, Mouaze D, Chaplin JR (2007) Air-water interface dynamic and free surface features in hydraulic jumps. Journal of Hydraulic Research, IAHR 45(5):679-685

Murzyn F, Chanson H (2009) Experimental investigation of bubbly flow and turbulence in hydraulic jumps. Environmental Fluid Mechanics 9(2):143-159. doi:10.1007/s10652-008-9077-4

Rajaratnam N (1962) An experimental study of air entrainment characteristics of the hydraulic jump. Journal of Institution Engineering India 42(7):247-273

Resch FJ, Leutheusser HJ (1972) Le ressaut hydraulique: mesure de turbulence dans la région diphasique. (The hydraulic jump: turbulence measurements in the two-phase flow region.) Journal La Houille Blanche 4:279-293 (in French).

Richard GL, Gavrilyuk SL (2013) The classical hydraulic jump in a model of shear shallow-water flows. Journal of Fluid Mechanics 725:492-521. doi:10.1017/jfm.2013.174

Rouse H, Siao TT, Nagaratnam S (1959) Turbulence characteristics of the hydraulic jump. Transactions ASCE 124:926-950

Schiebe F (1971) The stochastic characteristics of pressure fluctuations on a channel bed due to the turbulence in a hydraulic jump. PhD thesis, The University of Minnesota, Minneapolis, US

Thandaveswara BS (1974) Self aerated flow characteristics in developing zones and in hydraulic jumps. PhD thesis, Dept. of Civil Engineering, Indian Institute of Science, Bangalore, India, 399 pages.

Toso JW, Bowers CE (1988) Extreme pressures in hydraulic-jump stilling basins. Journal of Hydraulic Engineering 114(8):829-843

Valiani A (1997) Linear and angular momentum conservation in hydraulic jump. Journal of Hydraulic Research 35(3):323-354

Vasiliev OF, Bukreyev VI (1967) Statistical characteristics of pressure fluctuations in the region of hydraulic jump. Proceedings of the Congress – International Association for Hydraulic Research 2:1-8

Wang H, Chanson H (2014) Air entrainment and turbulent fluctuations in hydraulic jumps. Urban Water Journal. doi:10.1080/1573062X.2013.847464

Wang H, Felder S, Chanson H (2014a) An experimental study of turbulent two-phase flow in hydraulic jumps and application of a triple decomposition technique. Experiments in Fluids 55:1775. doi:10.1007/s00348-014-1775-8

Wang H, Murzyn F, Chanson H (2014b) Pressure, turbulence and two-phase flow measurements in hydraulic jumps. Hydraulic Model Report No. CH95/14, School of Civil Engineering, The University of Queensland, Brisbane, Australia, 81 pages

Wang H, Murzyn F, Chanson H (2014c) Total pressure fluctuations and two-phase flow turbulence in hydraulic jumps. Experiments in Fluids 55:1847. doi:10.1007/s00348-014-1847-9

Zhang G, Wang H, Chanson H (2013) Turbulence and aeration in hydraulic jumps: free-surface fluctuation and integral turbulent scale measurements. Environmental Fluid Mechanics 13(2):189–204. doi:10.1007/s10652-012-9254-3